Zero-field skyrmions generated via premartensitic transition in $Ni_{50}Mn_{35.2}In_{14.8}$ alloy

Shulan Zuo,[1,2] Feixiang Liang,[1,2] Ying Zhang,[1,*] Licong Peng,[1,2] Jiefu Xiong,[1,2] Yao Liu,[1,2] Rui Li,[1,2] Tongyun Zhao,[1] Jirong Sun,[1,2] Fengxia Hu,[1,2] and Baogen Shen[1,2,†]

[1]*State Key Laboratory of Magnetism, Institute of Physics, Chinese Academy of Sciences, Beijing 100190, People's Republic of China*

[2]*University of Chinese Academy of Sciences, Beijing 100049, People's Republic of China*

(Received 11 May 2018; published 18 October 2018)

Magnetic phase transition contributes to magnetocaloric effects and magnetoelastic coupling, producing significant multifunctions in Ni-based Heusler alloys. In this paper, the peculiar intermediate premartensitic phase during the transition from parent phase to martensite is identified in Ga-free $Ni_{50}Mn_{35.2}In_{14.8}$ alloy via Lorentz transmission electron microscopy combined with *in situ* magnetizing and cooling manipulation. The simultaneous coexistence of three skyrmion configurations at zero field in martensite is directly observed with correlation to the appearance of the intermediate magnetic phase and martensite twinning confinement. The evolution of magnetic domains demonstrates a mechanism to generate skyrmions with magnetization orientation adjusted via magnetic phase transition, which illustrates the associated physical properties.

DOI: 10.1103/PhysRevMaterials.2.104408

I. INTRODUCTION

Ni-Mn-Z (Z = Ga, Sn, Sb, In) materials are attractive multifunctional candidates for microelectronic actuation devices, hydraulic vaults, and magnetic sensing applications due to their interesting properties related to phase transition [1]. The anomaly of magnetoelastic coupling [2,3], thermal, and resistivity behaviors across the phase transition has been intensively investigated in Ni-Mn-Ga ferromagnetic shape memory alloys (FSMAs) [1–9]. A structural phase transition from a parent cubic austenite phase to a tetragonal martensitic phase together with a magnetic phase transition from paramagnetic to ferromagnetic state is usually expected while decreasing the temperature. A premartensitic state, referring to the intermediate state between the symmetric parent austenitic phase and a low-symmetry martensitic structure, shows approximately cubic symmetry with a micromodulated domain structure and weak first-order nature [1,4–6]. Many efforts via theoretical and experimental methods have indicated that the abundant physical properties are correlated with the origin of the premartensitic transition in Ni-Mn-Ga [3,7,10–13]. However, there are few reports about the identification of premartensitic transition in Ga-free FSMA, which could be a good candidate material due to its strong magnetoelastic coupling effects and lower cost [14]. Recently, via *in situ* optical microscope, the intermediate phase transition seems to have been detected in $Ni_{43}Mn_{41}Co_5Sn_{11}$ alloy [15,16] and $Ni_{50}Mn_{34}In_{15.5}Al_{0.5}$ alloy after applying external high pressure in the annealing fabrication process [14,17]. Although the Ni–Mn–In Heusler alloys have abundant physical properties, such as magnetic-field induced shape recovery effect, magnetothermal effect, elastocaloric effect, and so on [18–20], the delicate magnetic domain evolution of the premartensitic transition has not been comprehensively revealed yet.

Here, the dynamic behaviors of temperature-induced structural and magnetic phase transitions are extensively investigated in the $Ni_{50}Mn_{35.2}In_{14.8}$ alloy by using *in situ* Lorentz transmission electron microscopy (L-TEM). We present interesting magnetic structure evolution behaviors, including the clear identification of the premartensitic phase and the simultaneous generation of zero-field chiral skyrmions and biskyrmions during the phase transition. The direct experimental demonstration of these phase transitions in gallium-free ferromagnetic alloys is of great interest from the perspective of science and application [21]. The generation of skyrmions is proposed to be related to the magnetic anisotropy change and the intrinsic twinning features during the phase transition.

The topological spin textures of magnetic skyrmions have triggered enormous interest due to their significant performance and potential for spintronics applications [22]. Traditionally magnetic bubbles usually show random chirality in centrosymmetric materials [23]. The uniform fixed chirality in skyrmions is determined by the broken-symmetry structure in chiral magnets such as MnSi, FeCoSi, and FeGe endowed with Dzyaloshinskii-Moriya (DM) interactions [24–28]. In centrosymmetric magnets with uniaxial magnetic anisotropy, uniform biskyrmions with oppositely swirling spins and the same central spin polarity at the core sites have been explored [29,30]. The recent exploration of novel skyrmion materials and the discovery of new spin configurations of antiskyrmions [31,32] encouraged researchers to find more alternatives suitable for spintronic applications. These unique configurations are determined by the crystal structure and the competition of different magnetic interactions. Significant efforts have been underscored to generate zero-field nonvolatile skyrmions and to extend the temperature-field region via external manipulations or shape confinement [33–37] for the consideration of energy efficiency and operation convenience. In this paper, we

*Corresponding author: zhangy@iphy.ac.cn
†Corresponding author: shenbg@iphy.ac.cn

demonstrate simultaneous generation of three spin configurations of skyrmions with topological number +1, −1, and 2 at zero fields in correlation with the phase transition in Heusler $Ni_{50}Mn_{35.2}In_{14.8}$ alloy. The realization of different chiralities in zero-field skyrmions opens a way to manipulate skyrmions and to extend the topological functions of the traditional Heusler alloy.

II. EXPERIMENT

Polycrystalline $Ni_{50}Mn_{35.2}In_{14.8}$ alloy with nominal composition was prepared by arc-melting technique in high-purity argon atmosphere. Homogenization was achieved by sealing the ingots into quartz ampoules under argon atmosphere and annealing at 1073 K for 24 h, followed by quenching in ice water. The thin plate for the TEM observations was cut from the polycrystalline ingots and prepared via traditional mechanical polishing and argon-ion milling method. The observed grains are along the [001] zone axis after slight tilting. The magnetic domains were investigated using L-TEM (JEOL 2100F) operating at 200 kV. Via Fresnel L-TEM method, the magnetic domain walls are imaged as reversible bright or dark contrast depending on the defocus of the electron beam. In-focus images show more clearly structural contrast rather than magnetic domains. Quantitative in-plane magnetization maps were obtained based on the analyses of defocused Fresnel L-TEM images via the transport-of-intensity equation (TIE). *In situ* L-TEM observations of magnetic domain evolution under external fields were conducted using a liquid-nitrogen TEM holder (100–300 K). The objective lens was turned off when the sample holder was inserted and the perpendicular magnetic field was generated by increasing the current of the objective lens.

III. RESULTS AND DISCUSSION

The temperature dependence of magnetic phase evolution and crystal structure transition is systematically studied by L-TEM at zero field in correlation with the magnetization measurements in $Ni_{50}Mn_{35.2}In_{14.8}$ alloy as shown in Fig. 1. The small difference, between the ferromagnetic transition temperature T_C of around 306 K, extracted from the L-TEM observation, and the martensitic transformation temperature T_M of about 296 K, based on the *M*-*T* curves [Fig. 1(a)], indicates the considerable geometric effects between bulk and thin plate sample. The magnetic domains and the diffraction pattern [Figs. 1(c) and 1(e)] indicate the parent austenite phase at 293 K, which belongs to Cu_2MnAl-type $L2_1$-type bcc structure (space group $Fm\bar{3}m$, 225) with the lattice parameter about $a = 0.60$ nm, where Ni atoms preferentially occupy $8c(1/4, 1/4, 1/4)$ sites, Mn atoms occupy $4a(0, 0, 0)$ sites, and in off-stoichiometric cases extra Mn and In atoms occupy the $4b(1/2, 1/2, 1/2)$ sites as schematically shown in Fig. 1(b). The magnetic domain evolution is directly observed while decreasing temperatures and the corresponding selected area electron diffraction (SAED) indicate structural change along the [001] zone axis. The parallel lines with interval bright and black contrast demonstrate typical 180° magnetic domains with in-plane magnetization in the parent phase [Fig. 1(c)]. With decreasing temperature, the

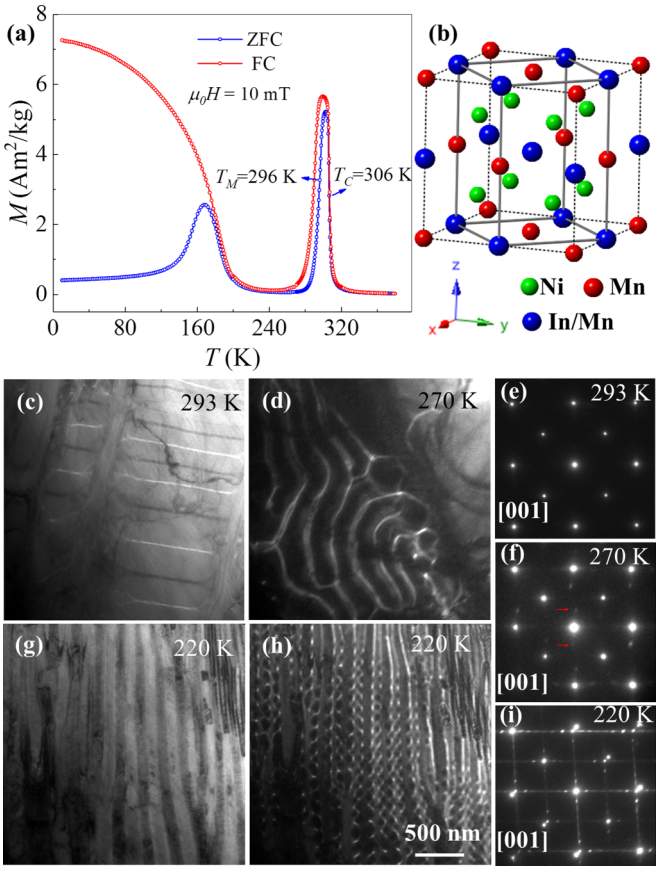

FIG. 1. Temperature dependency of microstructural and magnetic phase transition in $Ni_{50}Mn_{35.2}In_{14.8}$ alloy at zero field. (a) Temperature dependence of magnetization curves during zero-field cooling (ZFC) and field cooling (FC) measured at $\mu_0 H =$ 10 mT. (b) The schematic cubic $L2_1$ structure of parent austenite. Under-focus LTEM images of magnetic domain structures at different temperatures (c) 293 K, (d) 270 K, and (h) 220 K. (g) The in-focus image of the martensitic structure at 220 K. (c, f, i) The corresponding selected area electron diffraction (SAED) along the [001] zone axis, showing the crystal structure change from parent austenite phase at 293 K through intermediate phase at 270 K and to martensitic phase at 220 K. The red arrows indicate weak superlattice spots.

intermediate phase is observed showing magnetic stripe domains at 270 K [Fig. 1(d)]. The additional weak and diffuse streaks near the main diffraction spots as indicated by red arrows in the corresponding SAED [Fig. 1(f)] demonstrate similar cubic structures but with not-fully ordered superlattices while transforming from parent austenite to the intermediate phase [10,13]. As the temperature decreases to 220 K, the in-focus image with finely twinning structures [Fig. 1(g)] and the SAED with 7M modulation [Fig. 1(i)] confirm the nominally tetragonal martensite phase (space group *I*4/*mmm* with the lattice parameters $a = 0.41$ nm, $c = 0.69$ nm). Therefore, two successive structural transitions from cubic parent phase through intermediate phase to tetragonal martensite without breaking the center of symmetry are identified via the diffraction patterns while cooling down in $Ni_{50}Mn_{35.2}In_{14.8}$ alloy, like previous reports in Ni-Mn-Ga alloy [9,10,38]. The magnetic domains are simultaneously observed by changing

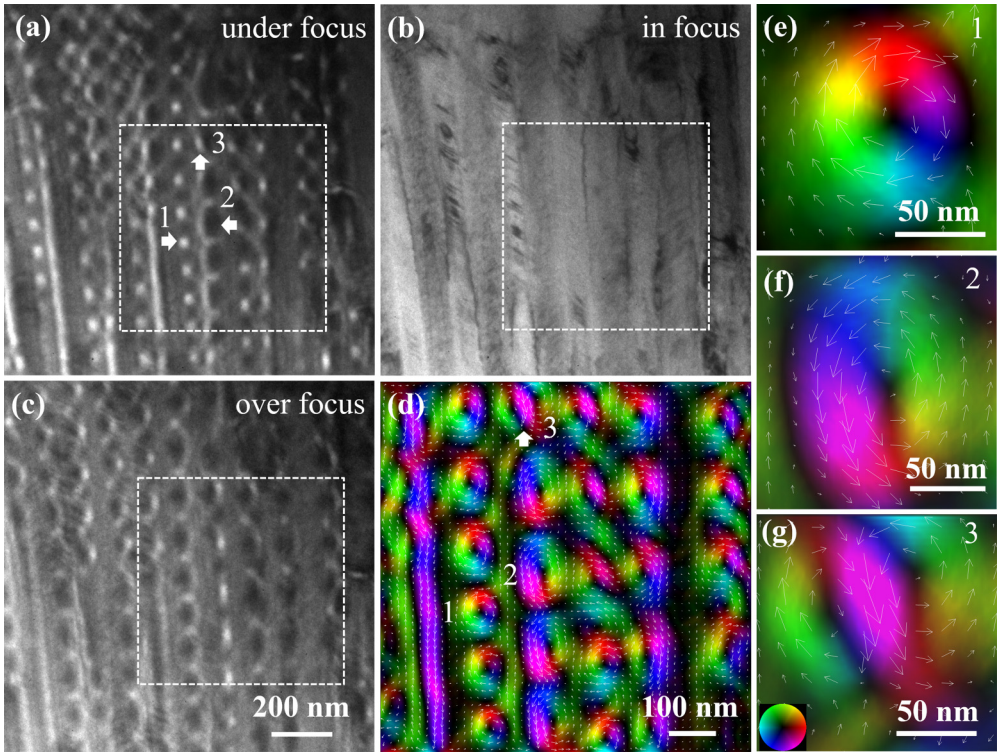

FIG. 2. Magnetic spin configurations of the nanoscale domains in $Ni_{50}Mn_{35.2}In_{14.8}$ alloy taken at zero magnetic field at 220 K. The corresponding (a) under-focus, (b) in-focus, and (c) over-focus L-TEM images showing magnetic domain distribution in the martensitic phase. (d) In-plane magnetization distribution map obtained by TIE analysis of the selected area showing the corresponding spin configurations of (a). (e)–(g) The enlarged spin textures for the single skyrmion as numbered in (a). The magnitude and orientation of the magnetization are depicted by the color and arrows as the color wheel in the inset.

the focus, revealing the rows of bright or black dots [Fig. 1(h)] in the martensitic phase. The magnetic domain evolution can be related to the changes of magnetocrystalline anisotropy and magnetic properties associated with phase transition [35]. The magnetic domains and crystal structures remain almost unchanged when the temperature is lower than 220 K.

The detailed magnetization textures at 220 K are further characterized via TIE analysis of under-focus, in-focus, and over-focus L-TEM images [Figs. 2(a)–2(c)] taken at zero field. The in-focus image in Fig. 2(b) shows clearer twinning structures from diffraction contrast than the defocused images. Three types of skyrmionlike spin configurations in Fig. 2(d) are extracted based on the reversed black and bright contrast in the defocused images. The corresponding in-plane magnetization distribution of the selected square area of Fig. 2(a) shows the skyrmion spin textures with clockwise helicity [Fig. 2(e)] and counterclockwise helicity [Fig. 2(f)] separately distributed along the twinning columns. The additional biskyrmion spin configuration [29,30] is detected in the region marked with a white arrow in Fig. 2(d) and enlarged in Fig. 2(g). Therefore, the L-TEM images with different bright and black contrast and the double contrast (black and white) in dots correspond to skyrmions and biskyrmions, respectively. The correlation between the skyrmion positions and the twinning features indicates that skyrmions with opposite helicities are confined along two interfaces of three mutually symmetric twinning structures. The different spin configurations like biskyrmions as marked with the arrow in Fig. 2(d) could also be introduced depending on the orientation and the size of the middle twinning. The energy competition among magnetic anisotropy, exchange energy, demagnetization energy, and other constraints could also affect the magnetization distribution. For example, the modulated uniaxial anisotropy of in-plane and out-of plane magnetization variation produced the skyrmions with one fixed helicity as previously reported in Ni_2MnGa [35]. In general terms, DM interaction is absent in NiMnIn alloy because of the consistent center of symmetry during the phase transition as discussed above in Fig. 1. The edge constraint of nanotwinning structure and its relative orientation together with the magnetization distribution could stabilize skyrmions at zero magnetic field. The shape confinement through fabricated patterns has been theoretically and experimentally proved to be an effective way to obtain skyrmions at zero field [35,39,40]. The discovery of zero-field skyrmions due to intrinsic twinning structure provides an option for skyrmion manipulation with significant energy efficiency.

Further magnetic domain evolution under perpendicular magnetic field is studied at 220 K as shown in Fig. 3. Based on the complicated magnetic domains with a mixture of skyrmions and biskyrmions at zero field [Fig. 3(a)], the perpendicular field is increased to 98 mT, and then the annihilation of skyrmions and biskyrmions in the thin region [Fig. 3(b)] uncovers the parallel domain walls. More skyrmions disappear as the magnetic field increases further to 164 mT [Fig. 3(c)]. The canted swirling magnetization in

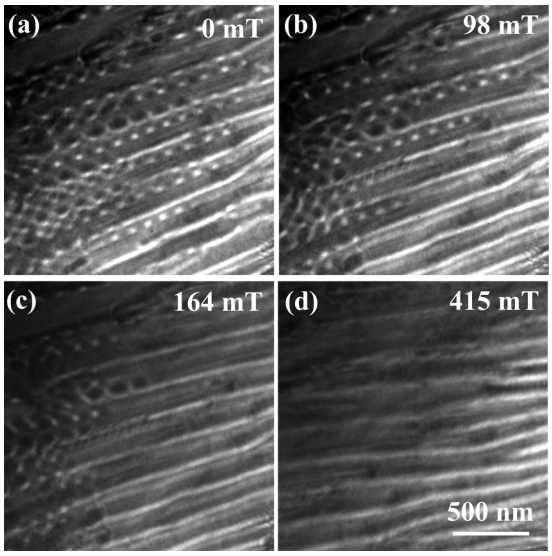

FIG. 3. The evolution of magnetic domains at 220 K in $Ni_{50}Mn_{35.2}In_{14.8}$ alloy while increasing the perpendicular magnetic fields to (a) 0 mT, (b) 98 mT, (c) 164 mT, and (d) 415 mT. The annihilation of magnetic skyrmions leaving behind the in-plane magnetization domain wall. The scale bar is 500 nm.

skyrmions is easier to be reoriented along the external perpendicular magnetic field than the in-plane magnetization. The skyrmions completely vanish at the magnetic field of about 415 mT, leaving the domain walls of in-plane magnetization as shown in Fig. 3(d). Compared to typical 180° domains with in-plane magnetization in the parent phase [Fig. 1(c)] at 293 K, the complicated magnetic domains indicate the diversified magnetization distribution in martensite [35]. The initial magnetic domains [Fig. 3(a)] can be recovered after switching off the magnetic field.

To understand the critical role of the intermediate phase in skyrmion generation, further magnetic domain evolution with repeated cooling and heating is demonstrated in Fig. 4. Different from sole 180° domains in Fig. 1(c), the additional stripe domains at 293 K [Fig. 4(a)] are introduced by previous cooling procedure due to thermal hysteresis, which is typical for the martensitic transition in Heusler alloy [17]. Further decreasing temperature to 280 K [Fig. 4(b)] below the martensitic transition $T_M \sim 296$ K, almost all 180° domains develop into stripe domains of the intermediate phase. As the temperature is further decreased, the martensitic features and diversified magnetic domains including skyrmions show up in Fig. 4(c). The martensitic phase has typical twinning structures due to the symmetry reduction [41,42] and the phase transition is verified by the appearance of extra modulated diffraction spots [Fig. 1(i)]. It should be noted that the intermediate stripe domains cannot be recovered at 293 K if heating temperature starts below the complete martensitic phase transition temperature of about 250 K. In order to sustain the intermediate stripe domain, the temperature has to be increased before the ultimate disappearance of stripe domains. In this way, stripe domains sustain to 302 K [Fig. 4(d)] during the heating process. Cooling from these mixed domains, the consecutive magnetic domain transition from stripe domains to dotlike skyrmions is observed as shown in Figs. 4(e)–4(g). The unchanged multivariate martensitic state with multiple twinning structures below ~261 K indicates that the martensitic transition is complete [Fig. 4(g)]. The significant hysteresis is observed by comparing the cooling process with

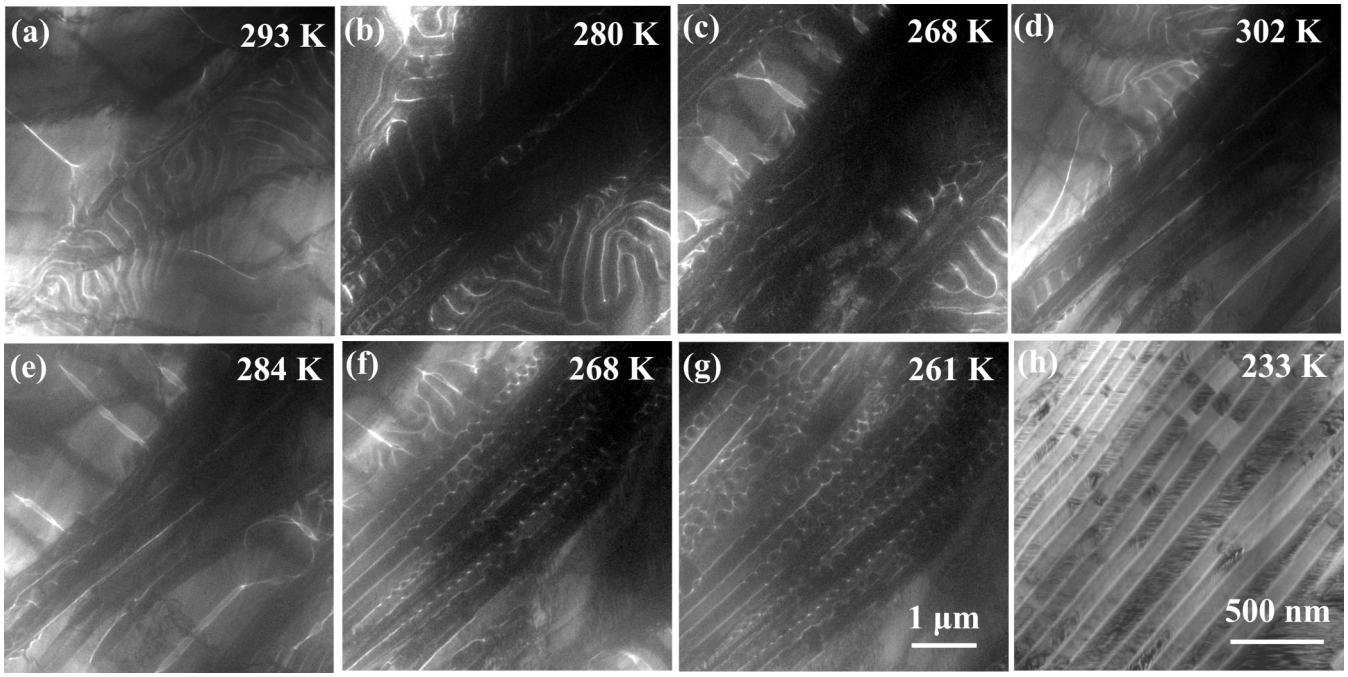

FIG. 4. The generation of the premartensitic phase and skyrmions in $Ni_{50}Mn_{35.2}In_{14.8}$ alloy at zero field by controlling the cooling and heating processes. The temperature dependency of intermediate stripe domain evolution during (a)–(c) the cooling process, (d) reheating, and (e)–(g) skyrmion generation in the second cooling process. (h) No skyrmions but common parallel magnetic domain walls along the grain boundary of the martensitic phase without going through intermediate stripe domains.

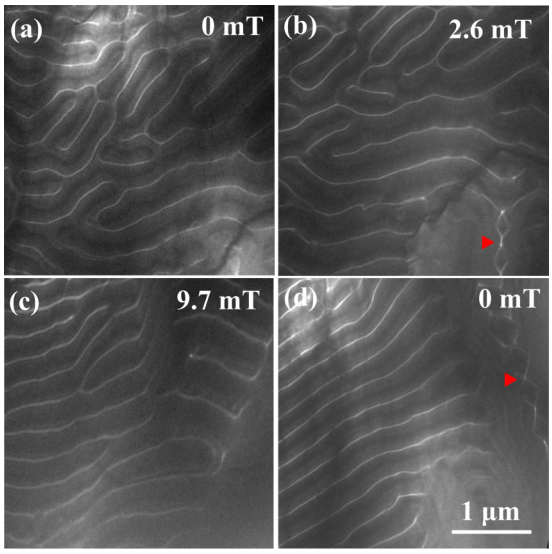

FIG. 5. The magnetic field dependency of intermediate stripe domains at 293 K in $Ni_{50}Mn_{35.2}In_{14.8}$ alloy at (a) 0 mT, (b) 2.6 mT, (c) 9.7 mT, and (d) back to 0 mT. The magnetic field is perpendicularly applied to the thin plate. The susceptible behavior of magnetic domains to the small magnetic field indicates the out-of-plane magnetization in the intermediate phase. The appearance of vortices marked by the red arrow confirms the competition between out-of-plane and in-plane magnetization.

the heating one during martensitic transition, which is consistent with the magnetic property measurements [Fig. 1(a)]. If no intermediate stripe domains sustain during the cooling procedure, no skyrmions but common magnetic domains along the boundary of the martensitic phase are produced as shown in Fig. 4(h). Thus, the appearance of the intermediate phase can be effectively controlled to produce skyrmions in NiMnIn alloy.

Out-of-plane magnetization develops in the transition from austenite to martensitic phase, which is represented in the stripe domains [43] of the intermediate phase by its dependency on small perpendicular magnetic fields in Fig. 5. By using the above preapplied cooling procedure, the stripe domains of the intermediate phase sustain at 293 K as shown in Fig. 5(a). The magnetic domains are easily altered by a very small magnetic field. As the field is increased to 9.7 mT, the stripe domain starts reorienting itself into parallel configuration. The appearance of vortices and antivortices at some locations as marked by red arrows further verifies the competition between out-of-plane and in-plane magnetization as illustrated and explained in previous single crystal $LaSrMnO_3$ [44]. All the magnetic domains vanish into a saturated ferromagnetic state at about 30 mT. The residual state after switching off the magnetic field shows the vortices and straightened domains in Fig. 5(d). The straightening effect may be driven by the Zeeman energy associated with the domain walls in an applied field, which occurs at much lower fields [43]. Therefore, the stripe domains of the intermediate phase are sensitive to external fields and have a narrow equilibrium temperature range, which makes it difficult to be detected during the experiments.

The magnetization distribution is susceptible to the energy competition during magnetic phase transition. It is considered that the competing of magnetic anisotropy and dipolar interaction contributes to the canted magnetization in the form of biskyrmions in centrosymmetric systems without DM interactions [29,30]. The modulated distribution of in-plane and out-of-plane magnetization in coordination with martensite twinning structure as previously illustrated [35] could be a major reason for the chiral skyrmions in this Heusler alloy. The existence of skyrmions at zero field seems to be related to the geometric confinement of nanotwinning structure in the martensitic phase. However, due to the complex phase transition, it is difficult to experimentally verify the comprehensive factors for the generation mechanism of chiral skyrmions in NiMnIn without further theoretical studies.

IV. CONCLUSIONS

In summary, the structural and magnetic transition from austenite to martensite is directly demonstrated with clear identification of the intermediate premartensitic phase by means of L-TEM in $Ni_{50}Mn_{35.2}In_{14.8}$ alloy. The simultaneous coexistence of three different skyrmion configurations in the absence of external magnetic field is produced due to the competition between in-plane and out-of-plane magnetization and the geometric confinement of intrinsic twinning structures in martensitic phase transition. The skyrmions are generated consistently with the appearance of the intermediate phase, revealing its critical role in skyrmion generation and in understanding the physical behavior across the martensitic transition. The realization of different chiral skyrmions opens up a possibility of skyrmion manipulation. Since $Ni_{50}Mn_{35.2}In_{14.8}$ is also ferroelastic, external strain/stress might become an alternative way to manipulate skyrmions as well.

ACKNOWLEDGMENTS

This work was supported by the National Key Research and Development Program of China (Grants No. 2017YFA0206300, No. 2016YFA0300701, No. 2016YFB0700902, No. 2016YFB0700903, and No. 2014CB643702), the National Natural Sciences Foundation of China (Grants No. 51590880, No. 51431009, and No. 11520101002), and the Youth Innovation Promotion Association, Chinese Academy of Sciences, Grant No. 2015004.

[1] Y. W. Ma, S. Awaji, K. Watanabe, M. Matsumoto, and N. Kobayashi, Appl. Phys. Lett. **76**, 37 (2000).

[2] A. Gonzalez-Comas, E. Obradó, L. Mañosa, A. Planes, V. A. Chernenko, B. J. Hattink, and A. Labarta, Phys. Rev. B **60**, 7085 (1999).

[3] A. Planes, E. Obradó, A. Gonzàlez-Comas, and L. Mañosa, Phys. Rev. Lett. **79**, 3926 (1997).

[4] V. V. Kokorin, V. A. Chernenko, E. Cesari, J. Pons, and C. Segui, J. Phys.: Condens. Matter **8**, 6457 (1996).

[5] A. Zheludev, S. M. Shapiro, P. Wochner, and L. E. Tanner, Phys. Rev. B **54**, 15045 (1996).
[6] M. A. Uijttewaal, T. Hickel, J. Neugebauer, M. E. Gruner, and P. Entel, Phys. Rev. Lett. **102**, 035702 (2009).
[7] A. Zheludev, S. M. Shapiro, P. Wochner, A. Schwartz, M. Wall, and L. E. Tanner, Phys. Rev. B **51**, 11310 (1995).
[8] J. H. Kim, F. Inaba, T. Fukuda, and T. Kakeshita, Acta Mater. **54**, 493 (2006).
[9] S. Singh, J. Bednarcik, S. R. Barman, C. Felser, and D. Pandey, Phys. Rev. B **92**, 054112 (2015).
[10] V. A. Chernenko, J. Pons, C. Segui, and E. Cesari, Acta Mater. **50**, 53 (2002).
[11] L. Manosa, A. Gonzalez-Comas, E. Obrado, A. Planes, V. A. Chernenko, V. V. Kokorin, and E. Cesari, Phys. Rev. B **55**, 11068 (1997).
[12] V. V. Kokorin, V. A. Chernenko, J. Pons, C. Segui, and E. Cesari, Solid State Commun. **101**, 7 (1997).
[13] H. S. Park, Y. Murakami, and D. Shindo, Appl. Phys. Lett. **83**, 3752 (2003).
[14] Y. Wu, S. Guo, S. Yu, H. Cheng, R. Wang, H. Xiao, L. Xu, R. Xiong, Y. Liu, Z. Xia, and C. Yang, Sci. Rep. **6**, 26068 (2016).
[15] S. C. Ma, H. C. Xuan, C. L. Zhang, L. Y. Wang, Q. Q. Cao, D. H. Wang, and Y. W. Du, Appl. Phys. Lett. **97**, 052506 (2010).
[16] S. C. Ma, D. H. Wang, Z. C. Zhong, J. M. Luo, J. L. Xu, and Y. W. Du, Appl. Phys. Lett. **102**, 032407 (2013).
[17] H. Cheng, Z. C. Xia, R. L. Wang, M. Wei, Z. Jin, S. Huang, C. Shang, H. Wu, X. X. Zhang, G. L. Xiao, and Z. W. Ouyang, J. Phys. D **50**, 135004 (2017).
[18] R. Kainuma, Y. Imano, W. Ito, Y. Sutou, H. Morito, S. Okamoto, O. Kitakami, K. Oikawa, A. Fujita, T. Kanomata, and K. Ishida, Nature (London) **439**, 957 (2006).
[19] T. Krenke, E. Duman, M. Acet, E. F. Wassermann, X. Moya, L. Manosa, A. Planes, E. Suard, and B. Ouladdiaf, Phys. Rev. B **75**, 104414 (2007).
[20] L. Mañosa, D. González-Alonso, A. Planes, E. Bonnot, M. Barrio, J.-L. Tamarit, S. Aksoy, and M. Acet, Nat. Mater. **9**, 478 (2010).
[21] Y. V. Kaletina, V. M. Schastlivtsev, and E. A. Fokina, Technical Phys. Lett. **39**, 529 (2013).
[22] N. Nagaosa and Y. Tokura, Nat. Nanotech. **8**, 899 (2013).
[23] X. Z. Yu, M. Mostovoy, Y. Tokunaga, W. Z. Zhang, K. Kimoto, Y. Matsui, Y. Kaneko, N. Nagaosa, and Y. Tokura, Proc. Natl. Acad. Sci. USA **109**, 8856 (2012).
[24] X. Z. Yu, N. Kanazawa, Y. Onose, K. Kimoto, W. Zhang, S. Ishiwata, Y. Matsui, and Y. Tokura, Nat. Mater. **10**, 106 (2011).
[25] T. Schulz, R. Ritz, A. Bauer, M. Halder, M. Wagner, C. Franz, C. Pfleiderer, K. Everschor, M. Garst, and A. Rosch, Nat. Phys. **8**, 301 (2012).
[26] S. X. Huang and C. L. Chien, Phys. Rev. Lett. **108**, 267201 (2012).
[27] X. Z. Yu, J. P. DeGrave, Y. Hara, T. Hara, S. Jin, and Y. Tokura, Nano Lett. **13**, 3755 (2013).
[28] X. Z. Yu, Y. Onose, N. Kanazawa, J. H. Park, J. H. Han, Y. Matsui, N. Nagaosa, and Y. Tokura, Nature (London) **465**, 901 (2010).
[29] X. Z. Yu, Y. Tokunaga, Y. Kaneko, W. Z. Zhang, K. Kimoto, Y. Matsui, Y. Taguchi, and Y. Tokura, Nat. Commun. **5**, 3198 (2014).
[30] W. H. Wang, Y. Zhang, G. Z. Xu, L. C. Peng, B. Ding, Y. Wang, Z. P. Hou, X. M. Zhang, X. Y. Li, E. K. Liu, S. G. Wang, J. W. Cai, F. W. Wang, J. Q. Li, F. X. Hu, G. H. Wu, B. G. Shen, and X. X. Zhang, Adv. Mater. **28**, 6887 (2016).
[31] A. K. Nayak, V. Kumar, T. Ma, P. Werner, E. Pippel, R. Sahoo, F. Damay, U. K. Rößler, C. Felser, and S. S. P. Parkin, Nature (London) **548**, 561 (2017).
[32] M. Hoffmann, B. Zimmermann, G. P. Müller, D. Schürhoff, N. S. Kiselev, C. Melcher, and S. Blügel, Nat. Commun. **8**, 308 (2017).
[33] L. Peng, Y. Zhang, W. Wang, M. He, L. Li, B. Ding, J. Li, Y. Sun, X. G. Zhang, J. Cai, S. Wang, G. Wu, and B. Shen, Nano Lett. **17**, 7075 (2017).
[34] S. Z. Lin, A. Saxena, and C. D. Batista, Phys. Rev. B **91**, 224407 (2015).
[35] C. Phatak, O. Heinonen, M. De Graef, and A. Petford-Long, Nano Lett. **16**, 4141 (2016).
[36] Y. Li, N. Kanazawa, X. Z. Yu, A. Tsukazaki, M. Kawasaki, M. Ichikawa, X. F. Jin, F. Kagawa, and Y. Tokura, Phys. Rev. Lett. **110**, 117202 (2013).
[37] K. Karube, J. S. White, D. Morikawa, M. Bartkowiak, A. Kikkawa, Y. Tokunaga, T. Arima, H. M. Rønnow, Y. Tokura, and Y. Taguchi, Phys. Rev. Mater. **1**, 074405 (2017).
[38] V. A. Chernenko, C. Segui, E. Cesari, J. Pons, and V. V. Kokorin, Phys. Rev. B **57**, 2659 (1998).
[39] M. Finazzi, M. Savoini, A. R. Khorsand, A. Tsukamoto, A. Itoh, L. Duò, A. Kirilyuk, Th. Rasing, and M. Ezawa, Phys. Rev. Lett. **110**, 177205 (2013).
[40] K. Y. Guslienko, IEEE Magnetics Lett. **6**, 4000104 (2015).
[41] M. Pitteri and G. Zanzotto, *Continuum Models for Phase Transitions and Twinning in Crystals* (CRC, Boca Raton, FL, 2002).
[42] K. Bhattacharya, *Microstructure of Martensite: Why it Forms and How it Gives Rise to the Shape-Memory Effect* (Oxford University, New York, 2003).
[43] A. Budruk, C. Phatak, A. K. Petford-Long, and M. De Graef, Acta Mater. **59**, 4895 (2011).
[44] X. Z. Yu, Y. Tokunaga, Y. Taguchi, and Y. Tokura, Adv. Mater. **29**, 1603958 (2016).